

PCCP

Accepted Manuscript



This is an *Accepted Manuscript*, which has been through the Royal Society of Chemistry peer review process and has been accepted for publication.

Accepted Manuscripts are published online shortly after acceptance, before technical editing, formatting and proof reading. Using this free service, authors can make their results available to the community, in citable form, before we publish the edited article. We will replace this *Accepted Manuscript* with the edited and formatted *Advance Article* as soon as it is available.

You can find more information about *Accepted Manuscripts* in the [Information for Authors](#).

Please note that technical editing may introduce minor changes to the text and/or graphics, which may alter content. The journal's standard [Terms & Conditions](#) and the [Ethical guidelines](#) still apply. In no event shall the Royal Society of Chemistry be held responsible for any errors or omissions in this *Accepted Manuscript* or any consequences arising from the use of any information it contains.



Cite this: DOI: 10.1039/xxxxxxxxxx

Coherent intensity fluctuation model for autocorrelation imaging spectroscopy with higher harmonic generating point scatterers — A comprehensive theoretical study[†]

Eli Slenders,^{*a‡} Martin vandeVen,^a Jef Hooyberghs,^{b,c} and Marcel Ameloot^a

Received Date

Accepted Date

DOI: 10.1039/xxxxxxxxxx

www.rsc.org/journalname

We present a general analytical model for the intensity fluctuation autocorrelation function for second and third harmonic generating point scatterers. Expressions are derived for a stationary laser beam and for scanning beam configurations for specific correlation methodologies. We discuss free translational diffusion in both three and two dimensions. At low particle concentrations, the expressions for fluorescence are retrieved, while at high particle concentrations a rescaling of the function parameters is required for a stationary illumination beam, provided that the phase shift per unit length of the beam equals zero.

Fluorescence correlation spectroscopy (FCS) has been widely used for several decades now to quantify ensemble dynamics.^{1,2} Applications on both the fundamental and applied level comprise the study of ligand binding to macromolecules³, protein aggregation in the cell membrane⁴ and molecular diffusion in solutions and living cells^{5,6}. Using laser scanning microscopy, the correlation spectroscopy technique was extended to account for both temporal and spatial correlations, which made it possible to determine slow membrane and cytoplasm dynamics^{7–12}, to quantify the cell surface receptor distribution¹³ and to map motility and flow velocity vectors.¹⁴

In FCS, information on the concentration and diffusion properties can be obtained by measuring the fluctuating emission intensity profile produced by the randomly moving fluorophores in the focal volume of the stationary laser beam¹⁵. Similarly, fluorescence fluctuation imaging in space and/or time comprises well-known methods such as Temporal Image Correlation Spectroscopy (TICS), SpatioTemporal Image Correlation Spectroscopy (STICS) and Raster Image Correlation Spectroscopy (RICS). In STICS^{13,14} microscopy images taken at a single region of interest are recorded repeatedly over a certain time span. These data are then correlated both in space and time, not only resulting in a translational diffusion coefficient value, but also in the char-

acterization of directed flow or motility present in the sample, enabling the construction of flow vector maps. Alternatively, in TICS, only the time correlation is considered for the various regions of the image¹⁵. The time information hidden in the motion of the scanning laser beam is explicitly used in RICS confocal measurements⁹. The dynamics of the moving particles determines the speeds selected for the scanning laser beam^{12,16,17}.

Even though fluorescence based methods carry advantages such as molecular specificity, a good contrast and single molecule sensitivity¹⁸, these are limited by several drawbacks: probes are sensitive to photobleaching and saturation^{18,19}, which restricts the illumination intensity and complicates the time-consuming study of slow processes, and intersystem crossing between excited singlet and triplet states, resulting in on/off-blinking²⁰. In addition, in general, a background signal due to the autofluorescence of the environment may overwhelm the fluorescence signal. This effect is especially apparent in biological materials, such as tissue, serum and blood²⁰ which contain a plethora of fluorescent molecules.

To the benefit of both applications and fundamental research, this conundrum of shortcomings can be overcome by using higher harmonic generating materials^{21–26}. Pantazis *et al.*²⁵ recently showed that tetragonal barium titanate (BaTiO₃) nanomaterial produces an extremely stable and strong second harmonic generated (SHG) signal *in vivo*. Liu *et al.*²⁰ made use of this same crystalline material in correlation spectroscopy experiments. Depending on the application, many other SHG active materials can be selected, such as KTiOPO₄^{27,28}, ZnO²⁸ and KNbO₃^{19,28}.

Numerous are the advantages in choosing the SHG approach over fluorescence based techniques. The instantaneous SHG light

^a Agoralaan, Bldg C, 3590 Diepenbeek, Belgium. Fax: +32 (0) 1126 9299; Tel: +32 (0) 1126 9233; E-mail: marcel.ameloot@uhasselt.be

^b Agoralaan, Bldg D, 3590 Diepenbeek, Belgium.

^c Boeretang, 200, 2400 Mol, Belgium.

[†] Electronic Supplementary Information (ESI) available: a pdf file with the detailed analytical derivation of the presented autocorrelation model. See DOI: 10.1039/b000000x/

has a high intensity, caused by the coherent nature of this non-linear scattering process²². SHG is typically not produced by the nanoparticle surrounding environment, thereby creating an optimal contrast in the recorded image. Demonstrated absence of photobleaching makes long-term imaging feasible, without degradation effects. Moreover, a flexible choice in the laser wavelength is combined with a narrow and well-defined wavelength of the SHG signal. As only a small amount of the incident light is absorbed by the SHG active particles²⁹, they do not heat up like metal nanoparticles³⁰. This is of particular interest when imaging delicate biological materials. Above all, SHG imaging makes label-free microscopy feasible, thus circumventing all limitations accompanying the use of probes^{22,25,31}. However, the critical component is the availability of non-clustering, uniform nanoparticles that avoid adverse effects such as the potential toxicity.

The SHG coherent scattering process can be described by expressing the induced sample polarization $\mathbf{P}(t)$ as a power series in the applied electric field strength vector $\mathbf{E}(t)$ under the assumption that the medium responds instantaneously^{32,33}:

$$\mathbf{P}(t) = \epsilon_0 \left[\chi^{(1)} \mathbf{E}(t) + \chi^{(2)} \mathbf{E}^2(t) + \chi^{(3)} \mathbf{E}^3(t) + \dots \right], \quad (1)$$

where ϵ_0 is the vacuum permittivity, $\chi^{(1)}$ is the scalar linear susceptibility, $\chi^{(2)}$ and $\chi^{(3)}$ are respectively second and third rank susceptibility tensors, $\mathbf{E}^2(t)$ can be represented as a column matrix containing all 9 permutations of $E_i E_j$ and $\mathbf{E}^3(t)$ all 27 permutations of $E_i E_j E_k$ with E_i , E_j and E_k the x, y and z component of $\mathbf{E}(t)$. The second and third term give rise to respectively a contribution of frequency 2ω (SHG) and 3ω (third harmonic generation, THG) under a sufficiently strong electric field of frequency ω ³².

For infinite centrosymmetric specimens, *i.e.* materials that exhibit perfect inversion symmetry, all $\chi^{(2n)}$ terms with $n \in \mathbb{N}$ in Eq. (1) vanish. Hence a monocrystal or other type of periodic structure must be non-centrosymmetric to produce a bulk SHG signal. For THG there is no such restriction.

In contrast to fluorescence, the emitted light produced by SHG and THG is coherent, with a possible phase mismatch between the photons, *e.g.* caused by the Gouy shift in a focused laser beam³⁴. Several papers describe the signal emanating from SHG samples as observed through a multiphoton microscope^{24,34–36}, but the interpretation of the autocorrelation function (ACF) of SHG/THG intensity fluctuations has so far been limited to a non-scanning laser beam^{19,37}.

Very recently rotational motion of nanodoublers has been observed in a cellular environment³⁸. Progress has been made in expanding theoretical aspects of SHG emission such as multipole contributions³⁹ and signals from ensembles of irregularly shaped nanoparticles⁴⁰. These building blocks will help to describe the complex dynamic behavior of possibly polydisperse, aggregating and corona protein covered nanoparticles in a crowded intracellular environment as observed by a strongly focused laser beam.

Here, we will partially rely on the work by Geissbuehler *et al.*¹⁹ to develop a general coherent Intensity Fluctuation Model (cIFM). The cIFM will allow to analytically describe the coherent counterparts of the fluorescence based methods FCS, TICS, STICS and RICS. A lowercase c in the acronyms stresses the coherent behavior of this process: coherent Correlation Spectroscopy (cCS), cTICS, cSTICS and cRICS respectively, pronounced as *e.g.* cohSTICS.

The spatial distribution of the illumination amplitude is in our model approximated by a 3D Gaussian function with a linear approximation of the Gouy phase shift across the focal volume in the direction of the beam. Although analysis of rotational diffusion of SHG particles has been described before^{38,41}, our representation does not account for the orientational dependence of the SHG signal. The theory is thus restricted to measurements in which the rotational dynamics are averaged out and uncoupled from the spatial movement, *e.g.* in a low viscosity medium. The point-particle assumption also restricts the theory to (nano)particles that are small enough to not feel a gradient in the illumination intensity.

In the following we develop first the expressions for the general cIFM. This will be the theoretical framework from which the analytical expressions of the ACFs of all coherent autocorrelation techniques described above will be derived. The comprehensive modular way in which the expressions are written allows to derive straightforwardly the formulas for special cases, such as the low and high particle concentration limit and 2D diffusion. An in-depth comparison with the fluorescence expressions is made. To gain an understanding of the influence of noise on the parameter retrieval in the fitting procedure of experimental data, simulated autocorrelation curves for a steady stationary illumination beam setup case are presented. This helps to ascertain the numerical stability of solutions against the appearance of parasitic local minima in the parameter optimization process that could lead to ambiguous conclusions on the obtained parameter values.

1 Theory

Consider a system of randomly diffusing non-interacting point particles illuminated by a Gaussian laser beam. Each particle scatters light at twice and three times the laser light frequency, with the electric field amplitude depending on the particle position. Let $I_q(\mathbf{r}, t)$ be the total detected far field intensity induced by all particles when position \mathbf{r} is imaged at time t . The index q reflects the order of the higher harmonic that is produced ($q = 2$ in SHG and $q = 3$ in THG). In a cSTICS, cRICS, cTICS or cCS measurement, the correlation between the intensity fluctuations in the microscopy images at different positions and/or time points can be described by the normalized ACF $G_q(\boldsymbol{\rho}, t)$ ⁴²:

$$G(\boldsymbol{\rho}, \tau) = \frac{\langle \delta I_q(\mathbf{r}_0, t) \delta I_q(\mathbf{r}_0 + \boldsymbol{\rho}, t + \tau) \rangle}{\langle I_q(\mathbf{r}_0, t) \rangle^2}, \quad (2)$$

where $\delta I_q(\mathbf{r}_0, t)$ is the fluctuating difference between the detected intensity at position \mathbf{r}_0 at time t and the mean intensity calculated over all positions and all time points. The brackets $\langle \cdot \rangle$ represent averaging, which can be, depending on the experimental configuration and data analysis, a temporal (cTICS and cCS) or spatiotemporal (cSTICS and cRICS) average. The quantities $\boldsymbol{\rho}$ and τ describe, respectively, the spatial and temporal lag between

two data points that are considered in the calculation of the ACF.

Eq. (2) can be rewritten into an equivalent, but computationally less demanding form:

$$G(\boldsymbol{\rho}, \tau) = \frac{\langle I_q(\mathbf{r}_0, t) I_q(\mathbf{r}_0 + \boldsymbol{\rho}, t + \tau) \rangle - \langle I_q(\mathbf{r}_0, t) \rangle^2}{\langle I_q(\mathbf{r}_0, t) \rangle^2}, \quad (3)$$

The calculation of the intensity $I_q(\mathbf{r}, t)$ is based on the assumption of a Gaussian focal volume with $1/e^2$ beam waist ω_0 in the radial direction and z_0 in the axial direction. The axial Gouy phase shift is approximated to be linear, *i.e.* a constant shift per unit length, κ_q ¹⁹. The amplitude and phase of the electric field of the focused laser beam is then given by Eq. (4)³³:

$$A_q(\mathbf{r}) = A_{q0} \exp\left(-\frac{x^2 + y^2}{\omega_0^2/q}\right) \exp\left(-\frac{z^2}{z_0^2/q}\right) \exp(-i\kappa_q z), \quad (4)$$

with A_{q0} the maximum electric field amplitude produced by the light source. In this coordinate system, the x - and y -axis are within the focal plane and the z -axis is along the laser beam propagation, with the focus of the laser beam at $x = 0, y = 0, z = 0$.

The intensity observed for a laser beam at position \mathbf{r}_0 is then calculated as⁴³:

$$I_q(\mathbf{r}_0, t) = \left| \chi^{(q)} \right|^2 \left| \int A_q(\mathbf{r} - \mathbf{r}_0) c(\mathbf{r}, t) dV \right|^2. \quad (5)$$

Here, $\chi^{(q)}$ is the dielectric susceptibility tensor and dV is the shorthand notation for the cubic volume element $dx dy dz$. The assumed infinitely small particles are represented by a positional and time dependent particle density function $c(\mathbf{r}, t)$, which is a sum of Dirac delta functions⁵. Since $A_q(\mathbf{r})$ is an even function in x and y and because of the symmetry in the z -direction after taking the squared modulus to calculate the intensity, the integral can be interpreted as the convolution of $A_q(\mathbf{r})$ with $c(\mathbf{r}, t)$.

2 Results

The comprehensive details of the ACF for point scattering particles exhibiting free translational diffusion is given in the Supplementary Information. The general solution to the cIFM is a sum of 29 terms of which 12 cancel out and 8 terms are zero for symmetry reasons. The resulting 9 terms are split into 3 groups, denoted with the letters A, B and C to emphasize their similar origin:

$$G(\boldsymbol{\rho}, \tau) = (A3 + A4 + A5 + A7 + B6 + B7 + B9 + C5 + C7)/G_N, \quad (6)$$

where G_N is the normalization factor, $\langle I_q(\mathbf{r}_0, t) \rangle^2$ as in Eq. (2).

All terms of the numerator are functions of the system parameters ω_0 , z_0 and κ_q , and the sample parameters N , the average number of particles in the focal volume, as well as D , the translational diffusion coefficient. The spatial evolution of G is plotted in Fig. 1 for typical parameter values. The peak height is directly related to the concentration of the scatterers; the higher the particle density, the lower $G(\mathbf{0}, t)$. The peak width of G decreases with an increasing diffusion coefficient value and the height drops for increasing time lags in a similar way as for 1-photon fluores-

cence¹⁵, although the absolute values can differ significantly⁴⁴. This fact proves that one cannot simply use the fluorescence expressions to fit experimental data from SHG particles to obtain information about the concentration and the diffusion rate. In the following we briefly list modifications to be made to the cIFM for the specific approaches listed above. We also explore the low and high particle concentration limits. Attention is paid to the specific case of 2D diffusion as well.

2.1 cSTICS

To adapt the general cIFM for cSTICS type measurements, one must discretize the spatial variables in the expressions to simulate the pixel structure of a digital image. This includes one substitution in the cIFM: $\boldsymbol{\rho} = (\rho_x, \rho_y, \rho_z) = (\delta r \xi, \delta r \psi, \delta s \phi)$ with δr and δs the pixel size in the lateral and axial direction and ξ , ψ and ϕ the pixel number in the x -, y - and z -direction respectively.

2.2 cRICS

In cRICS, a laser beam scans each pixel sequentially in a raster pattern to obtain a complete image. This results in a definite relation between the spatial and temporal part of the equation, depending on the experimental settings: $G(\boldsymbol{\rho}, \tau)$ becomes now an implicit function of time only, $G(\boldsymbol{\tau}(\boldsymbol{\rho}))$, with $\boldsymbol{\tau}(\boldsymbol{\rho}) = \rho_x \tau_x + \rho_y \tau_y + \rho_z \tau_z = \boldsymbol{\rho} \cdot \boldsymbol{\tau}$. Everywhere in Eq. (6), the substitution $\boldsymbol{\tau} = \boldsymbol{\rho} \cdot \boldsymbol{\tau}$ must be made, with $\boldsymbol{\tau}$ a 3 dimensional constant vector containing respectively the pixel dwell time, the line scan time and the frame time (units of time/length). Consider as an example a typical 2D frame scan of 1024x1024 pixels with a field of view of 300x300 μm^2 and with a scan speed of 15 seconds for a complete image. This is about 14.3 $\mu\text{s}/\text{pixel}$, 14.6 ms/line and 15 s/frame , or equivalently, 48.8 s/m in the x -direction, 49.8e3 s/m in the y -direction and no z -direction scan time. The vector $\boldsymbol{\tau}$ is then (48.8, 49.8e3, 0).

2.3 cTICS and cCS

For a steady laser beam, the spatial information can be omitted from the cIFM ($\boldsymbol{\rho} = 0$) resulting in a much more compact ACF $G_q(\tau)$. Evidently, the same expression can be used in cTICS. In Fig. 2 a comparison with the corresponding fluorescence expression for the same parameter values is plotted, indicating that the difference between the two techniques can be significant. Similarly to Fig. 1, one can observe the effect of the coherence of the SHG signal by comparing the SHG and the fluorescence curve. Geissbuehler *et al.*¹⁹ performed directly this restricted derivation, but, as shown in this same Fig. 2, our results are different. This discrepancy is caused by the omission of the B and C labeled terms and a term in the denominator in the cited article.

2.4 Diffusion with flow

The cIFM of Eq. (6) can readily be adjusted for diffusion with flow. The approach taken in the Supplementary Information can be intuitively understood as follows. Consider a 1-dimensional system of particles freely diffusing in the x -direction. The ACF $G(\rho_x)$ then relates each point x with the point $x + \rho_x$. On average,

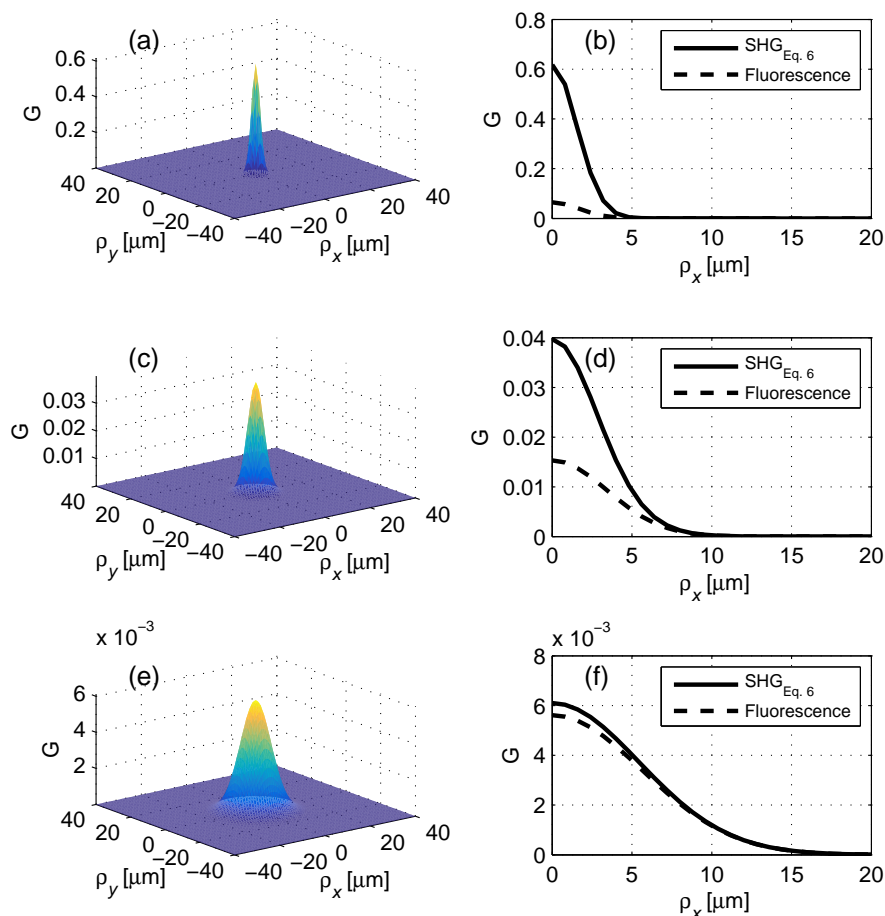


Fig. 1 Plots of the ACF with respect to the lateral spatial shift ρ_x and ρ_y in a cSTICS simulation for time lags $\tau = 1$ s (a)–(b), $\tau = 10$ s (c)–(d) and $\tau = 30$ s (e)–(f). The parameter values are $\omega_0 = 2.7 \mu\text{m}$, $z_0 = 54 \mu\text{m}$, $N = 10$, $D = 0.5 \mu\text{m}^2/\text{s}$ and $\kappa_q = 0.3276 \mu\text{m}^{-1}$, similarly to the value used in¹⁹. The left panels show 3D plots of the temporal evolution of the SHG ACF. In the right panels the ACF cross section $\rho_y = 0$ is plotted, as well as a comparison with the corresponding fluorescence ACF. Since the SHG focal volume is a factor of $\sqrt{2}$ smaller in all directions compared to 1-photon fluorescence, the beam parameters for the fluorescence curves were adjusted to $\omega_0/\sqrt{2}$ and $z_0/\sqrt{2}$ to obtain the same focal volume. The same figure with $\kappa_q = 0$ is plotted in the Supplementary Information for comparison.

the distance between the beam position at $x + \rho_x$ and the particles that were imaged at position x is equal to ρ_x . However, if there is a flow component v_x present, this distance decreases by an amount of $v_x \tau$ with τ the time lag between the imaging of the two points. An analogous argument can be made in 3 dimensions, leading to the following substitutions for each component of $\boldsymbol{\rho}$ in Eq. (6): $\rho_x \rightarrow \rho_x - v_x \tau$, $\rho_y \rightarrow \rho_y - v_y \tau$ and $\rho_z \rightarrow \rho_z - v_z \tau$.

2.5 Low particle concentration limit

It is particularly interesting to investigate the behavior of Eq. (6) in the limit of a very low particle concentration, where the resulting expression will not depend on the phase shift per unit length κ_q , since the phase information is not relevant. For $N \ll 1$ the only terms that remain are the ones containing the smallest exponent of N , *i.e.* A7, B9 and C7. Hence the autocorrelation is reduced to:

$$G(\boldsymbol{\rho}, \tau) = (A7 + B9 + C7)/G'_N, \quad (7)$$

with $G'_N = N^2/8$. The full expression for 3D diffusion is:

$$G(\boldsymbol{\rho}, \tau) = \frac{\exp\left(-\frac{q(\rho_x^2 + \rho_y^2)}{4qD\tau + \omega_0^2} - \frac{q\rho_z^2}{4qD\tau + z_0^2}\right)}{N\left(\frac{4qD\tau}{\omega_0^2} + 1\right)\sqrt{\frac{4qD\tau}{z_0^2} + 1}} \quad (8)$$

Notice that the parameter κ_q is — as expected — not appearing in the equation. Indeed, when N is small, the probability of multiple scatterers simultaneously being located inside the illumination volume is negligible. The coherent nature, and consequently the phase information of the scattered light, becomes irrelevant.

Eq. (8) is the same equation as obtained in the fluorescence intensity fluctuation model. Evidently then, one can find the expressions for the several correlation spectroscopy methodologies by using the appropriate substitutions. For $q = 1$, *i.e.* 1-photon illumination, $\rho_x = \delta r \xi - v_x \tau$, $\rho_y = \delta r \psi - v_y \tau$ and $\rho_z = \delta s \phi - v_z \tau$, Eq. (8) is the exact same equation as the STICS ACF¹⁴, with δr , δs , ξ , ψ and ϕ as defined earlier. The spatial and temporal

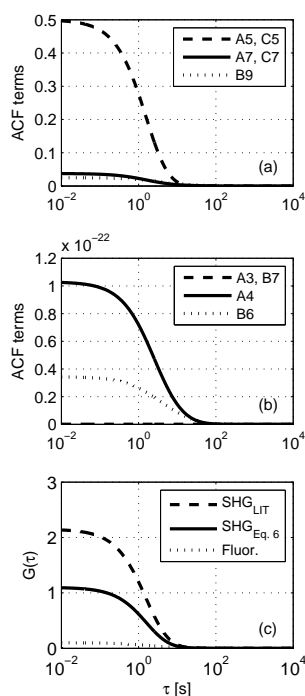


Fig. 2 Plots of the ACF with respect to the temporal shift, using the same parameter values as in Fig. 1. All nine terms of Eq. (6) that contribute to the ACF curve are plotted (a–b), as well as the total ACF, a comparison with the literature model used¹⁹ (SHG_{LIT}) and the fluorescence expression (Fluor.) in (c). Note that for these parameter values, there is a huge difference in the order of magnitude between the terms of (a) and (b); the latter group can safely be ignored in this case for the total ACF calculation.

variables ρ and τ can be coupled as before with the substitution $\tau = \rho \cdot \tau$ to obtain the RICS expression. Evaluating Eq. (8) for a stationary beam ($\rho = 0$) yields the FCS expression for free diffusion and the substitutions $\rho_x = v_x \tau$, $\rho_y = v_y \tau$ and $\rho_z = v_z \tau$ can be used as before to study diffusion with flow. Note that the minus signs can be omitted here, since only the squared values appear in Eq. (8). All results in this paragraph apply to 2-photon excitation fluorescence as well by substitution of $q = 2$.

These results prove that for very dilute suspensions, there is essentially no difference between the signal obtained from fluorescent emitters and higher harmonic generating scatterers. The simulated graphs of Fig. 3 show that for $N < 0.1$ the fluorescence autocorrelation curve deviates less than 10% from the SHG curve. For larger values of N , one must use the SHG expressions, since the difference with the fluorescence formula will become too large to get reliable fit results, see Fig. 3 (c).

2.6 High particle concentration limit

When evaluating Eq. (6) in the limit of a large value for N , the only left over term in the numerator is A3:

$$G(\rho, \tau) = \frac{A3}{G_N''} \quad (9)$$

with G_N'' an adjusted normalization factor, dependent on parti-

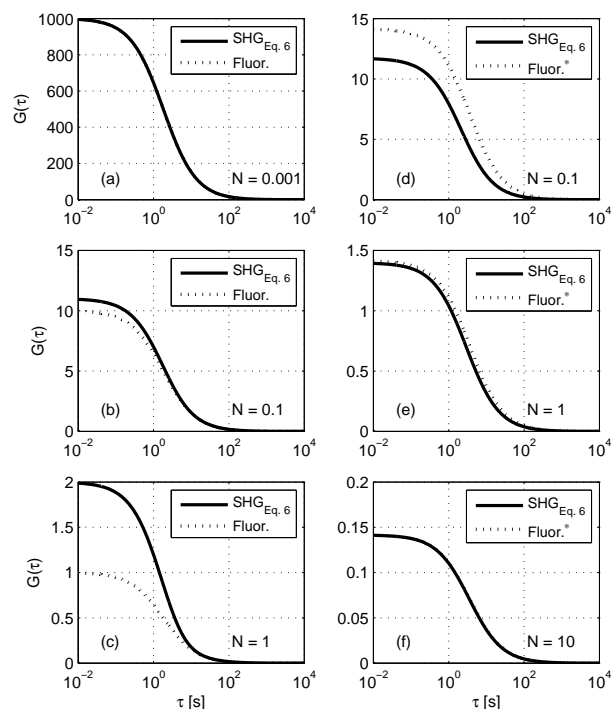


Fig. 3 Comparison between the SHG and fluorescence autocorrelation functions. The left graphs indicate the low particle limit for the SHG ($\kappa_q = 0.3276 \mu\text{m}^{-1}$) and the fluorescence expressions using the same parameter values as in the legend of Fig. 1. The graphs on the right compare the high particle limit for the SHG ($\kappa_q = 0 \mu\text{m}^{-1}$) and fluorescence (Fluor.*) expressions, calculated with half the diffusion coefficient ($D/2$) and a lower particle concentration ($N/\sqrt{2}$), as denoted by the asterisk. One can readily observe the convergence of the SHG and fluorescence expressions in both limits.

cle concentration, z_0 , κ_q and q . In a non-scanning system with a negligibly low Gouy phase factor value, this simplifies to:

$$G(\tau) = \frac{\sqrt{2}}{N} \frac{1}{N \left(\frac{2qD\tau}{\omega_0^2} + 1 \right) \sqrt{\frac{2qD\tau}{z_0^2} + 1}} \quad (10)$$

This is formally equivalent to the fluorescence expression under 1-photon excitation, when substituting $q = 1$, $N = \sqrt{2}N_F$ and $D = 2D_F$, where the index F denotes the corresponding parameter for the fluorescent case. It can be noted that this simple rescaling cannot be used for the scanning implementations.

2.7 2D diffusion

The full expressions of all terms of the cIFM are written in such a way that one can straightforwardly retrieve from which integration each factor is coming. This allows one to obtain the formulas for a 2D system in a convenient way. Assume in this case that the excitation beam is perpendicular to the 2D movement of the particles. Now, one can simply remove all factors in brackets and all terms in exponents that contain z_0 . The result is a sum of A terms only. Gassin *et al.*³⁷ derived directly the 2D ACF, but, unlike our expression, the proposed equation does not converge to the fluorescence model in the low particle limit.

2.8 Sensitivity to noise for parameter retrieval

In a typical autocorrelation spectroscopy experiment, the $1/e^2$ beam waist in the lateral direction ω_0 and in the axial direction z_0 are known parameters and kept constant when the diffusion coefficient D and the particle concentration c are fitted. In order to check the fit stability of the parameter retrieval process for SHG/THG, several computer simulations for 3D diffusion (see Supplementary Information) were performed using the theoretical autocorrelation expression for cCS and typical experimental settings. Random noise was added to theoretical curve and the resulting data were then fitted with the analytical equation. The starting values for the concentration and the translational diffusion fit parameters c and D were randomly chosen between 1/10 and 10 times the original value. This process was repeated 1000 times for each noise level. Fig. 4 shows the results. One can immediately conclude that — although the spread in the retrieved values increases with the noise level — the fit procedure will on average retrieve the original value of c and D . When κ_q is left as a freely adjustable fit parameter, however, the additional degree of freedom creates a high probability of ending up in a local minimum far away from the set values, as illustrated in the Supplementary Information. We therefore recommend to estimate κ_q beforehand⁴⁴ from the known optical configuration and keep this parameter fixed during the fitting procedure.

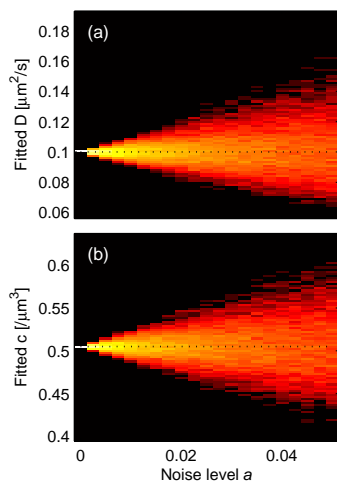


Fig. 4 2D histograms of the fit results obtained by fitting 1000 simulated ACFs for 21 noise levels using the following parameter values: $\omega_0 = 0.32 \mu\text{m}$, $z_0 = 0.982 \mu\text{m}$, $c = 0.505 \mu\text{m}^{-3}$, $D = 0.1 \mu\text{m}^2/\text{s}$ and $\kappa_q = 0.249 \mu\text{m}^{-1}$. The pixel color represents the number of fits that ended up in that voxel (black = 0, white = 1000). The black dashed line indicates the simulation value. In a simultaneous fit of the diffusion coefficient (a) and the concentration (b), both parameters reproduce the exact value for a noiseless ACF. The spread in the recovered values increases with the noise level, but due to the symmetry, it is possible to average the results over multiple data sets.

3 Conclusions

The numerous shortcomings of FCS and fluorescence based image correlation spectroscopy methods can be overcome by using SHG and THG materials. However, the fluorescence theory does not account for the coherent aspect of this scattering phenomenon.

We show that the recently published restricted SHG and THG derivations should be expanded and corrected. In future work, these theoretical observations will be validated on model systems in an experimental setup.

Acknowledgements

This research has been funded by the Interuniversity Attraction Poles Program (IAP FS2 P7/05, Functional Supramolecular Systems) initiated by the Belgian Science Policy Office.

Supplementary Information

The full derivation of the autocorrelation function for cSTICS, cRICS, cTICS, cCS, with and without flow, 3D and 2D diffusion, the low and high particle concentration limit and the fit procedure of the simulation data can be found in the Supplementary Information.

References

- 1 J. Enderlein, *Pure Appl. Chem.*, 2013, **85**, 999–1016.
- 2 E. Elson, R. Rigler and E. S. Elson, in *Fluorescence correlation spectroscopy - Theory and applications - Introduction*, Springer-Verlag Berlin, Berlin, 2001, vol. 65, pp. 1–6.
- 3 E. L. Elson and D. Magde, *Biopolym.*, 1974, **13**, 1–27.
- 4 K. M. Berland, P. T. C. So and E. Gratton, *Biophys. J.*, 1995, **68**, 694–701.
- 5 A. G. Palmer and N. L. Thompson, *Biophys. J.*, 1987, **52**, 257–270.
- 6 R. Brock, M. A. Hink and T. M. Jovin, *Biophys. J.*, 1998, **75**, 2547–2557.
- 7 N. O. Petersen, *Biophys. J.*, 1986, **49**, 809–815.
- 8 K. M. Berland, P. T. C. So, Y. Chen, W. W. Mantulin and E. Gratton, *Biophys. J.*, 1996, **71**, 410–420.
- 9 M. A. Digman, P. Sengupta, P. W. Wiseman, C. M. Brown, A. R. Horwitz and E. Gratton, *Biophys. J.*, 2005, **88**, L33–L36.
- 10 J. Ries and P. Schwille, *Biophys. J.*, 2006, **91**, 1915–1924.
- 11 J. Ries, S. Chiantia and P. Schwille, *Biophys. J.*, 2009, **96**, 1999–2008.
- 12 E. Gielen, N. Smisdom, M. vandeVen, B. De Clercq, E. Gratton, M. Digman, J. M. Rigo, J. Hofkens, Y. Engelborghs and M. Ameloot, *Langmuir*, 2009, **25**, 5209–5218.
- 13 N. O. Petersen, P. L. Hoddellius, P. W. Wiseman, O. Seger and K. E. Magnusson, *Biophys. J.*, 1993, **65**, 1135–1146.
- 14 B. Hebert, S. Costantino and P. W. Wiseman, *Biophys. J.*, 2005, **88**, 3601–3614.
- 15 P. W. Wiseman, *Methods Enzymol.*, 2013, **518**, 245–267.
- 16 M. A. Digman, C. M. Brown, P. Sengupta, P. W. Wiseman, A. R. Horwitz and E. Gratton, *Biophys. J.*, 2005, **89**, 1317–1327.
- 17 E. Gielen, N. Smisdom, B. De Clercq, M. vandeVen, R. Gijssbers, Z. Debyser, J. M. Rigo, J. Hofkens, Y. Engelborghs and M. Ameloot, *J. Fluoresc.*, 2008, **18**, 813–819.
- 18 S. Broillet, A. Sato, S. Geissbuehler, C. Pache, A. Bouwens, T. Lasser and M. Leutenegger, *Opt. Express*, 2014, **22**, 782–802.
- 19 M. Geissbuehler, L. Bonacina, V. Shcheslavskiy, N. L. Boc-

- chio, S. Geissbuehler, M. Leutenegger, I. Marki, J. P. Wolf and T. Lasser, *Nano Lett.*, 2012, **12**, 1668–1672.
- 20 J. Liu and J. Irudayaraj, *Opt. Express*, 2013, **21**, 27063–27073.
- 21 P. J. Campagnola, M. D. Wei, A. Lewis and L. M. Loew, *Biophys. J.*, 1999, **77**, 3341–3349.
- 22 P. Campagnola, *Anal. Chem.*, 2011, **83**, 3224–3231.
- 23 P. J. Campagnola, H. A. Clark, W. A. Mohler, A. Lewis and L. M. Loew, *J. Biomed. Opt.*, 2001, **6**, 277–286.
- 24 C. L. Hsieh, Y. Pu, R. Grange and D. Psaltis, *Opt. Express*, 2010, **18**, 11917–11932.
- 25 P. Pantazis, J. Maloney, D. Wu and S. E. Fraser, *Proc. Natl. Acad. Sci. U.S.A.*, 2010, **107**, 14535–14540.
- 26 D. Debarre, W. Supatto, A. M. Pena, A. Fabre, T. Tordjmann, L. Combettes, M. C. Schanne-Klein and E. Beaurepaire, *Nat. Methods*, 2006, **3**, 47–53.
- 27 L. Mayer, A. Slablab, G. Dantelle, V. Jacques, A. M. Lepagnol-Bestel, S. Perruchas, P. Spinicelli, A. Thomas, D. Chauvat, M. Simonneau, T. Gacoin and J. F. Roch, *Nanoscale*, 2013, **5**, 8466–8471.
- 28 D. Staedler, T. Magouroux, R. Hadji, C. Joulaud, J. Extermann, S. Schwungi, S. Passemard, C. Kasparian, G. Clarke, M. Gerrmann, R. Le Dantec, Y. Mugnier, D. Rytz, D. Ciepielewski, C. Galez, S. Gerber-Lemaire, L. Juillerat-Jeanneret, L. Bonacina and J. P. Wolf, *ACS Nano*, 2012, **6**, 2542–2549.
- 29 Z. L. Tang, D. Xing and S. H. Liu, *Sci. China Ser. G-Phys. Astron.*, 2004, **47**, 8–16.
- 30 Y. Garbovskiy, O. Zribi and A. Glushchenko, in *Emerging applications of ferroelectric nanoparticles in materials technologies, biology and medicine*, InTech, 2012, book section 21, pp. 475–497.
- 31 R. Paesen, K. Sanen, N. Smisdom, L. Michiels and M. Ameloot, *Acta Biomater.*, 2014, **10**, 2036–2042.
- 32 R. W. Boyd, *Nonlinear Optics, 3rd Edition*, Elsevier Academic Press Inc., San Diego, 2008, pp. 1–613.
- 33 L. Novotny and B. Hecht, *Principles of Nano-Optics*, Cambridge University Press, 2006.
- 34 R. Dzakpasu and D. Axelrod, *Biophys. J.*, 2004, **87**, 1279–1287.
- 35 J. Mertz and L. Moreaux, *Opt. Commun.*, 2001, **196**, 325–330.
- 36 E. Y. S. Yew and C. J. R. Sheppard, *Opt. Express*, 2006, **14**, 1167–1174.
- 37 P. M. Gassin, G. Martin-Gassin, E. Benichou and P. F. Brevet, *J. Phys. Chem. C*, 2014, **118**, 1135–1141.
- 38 C. Macias-Romero, M. E. P. Didier, V. Zubkovs, L. Delannoy, F. Dutto, A. Radenovic and S. Roke, *Nano Lett.*, 2014, **14**, 2552–2557.
- 39 J. I. Dadap, J. Shan and T. F. Heinz, *J. Opt. Soc. Am. B-Opt. Phys.*, 2004, **21**, 1328–1347.
- 40 A. G. F. de Beer, S. Roke and J. I. Dadap, *J. Opt. Soc. Am. B-Opt. Phys.*, 2011, **28**, 1374–1384.
- 41 E. C. Y. Yan and K. B. Eisenthal, *J. Phys. Chem. B*, 2000, **104**, 6686–6689.
- 42 D. E. Koppel, D. Axelrod, J. Schlessinger, E. L. Elson and W. W. Webb, *Biophys. J.*, 1976, **16**, 1315–1329.
- 43 J. X. Cheng, E. Potma and S. X. Xie, *J. Phys. Chem. A*, 2002, **106**, 8561–8568.
- 44 P. W. Wiseman and N. O. Petersen, *Biophys. J.*, 1999, **76**, 963–977.